ACS Photonics

pubs.acs.org/journal/apchd5

Letter

Low-Threshold Continuous-Wave Anti-Stokes Raman Lasing in Silicon Racetrack Resonators

Yaojing Zhang,* Keyi Zhong, Wen Zhou, and Hon Ki Tsang*

Cite This: https://doi.org/10.1021/acsphotonics.1c01326

Read Online

ACCESS | Metrics & More | Article Recommendations | Supporting Information

ABSTRACT: We report the first experimental observation of continuous-wave anti-Stokes Raman lasing in a reverse-biased 2.8 mm long multimode silicon racetrack resonator with high quality factors (>10^6) at all the pump, Stokes, and anti-Stokes wavelengths. The anti-Stokes laser has a milliwatt pump threshold power. The laser output power is linearly proportional to both the Stokes output power and the pump power. The Stokes output power becomes saturated at higher pump powers and limits the maximum output power of the anti-Stokes wave. Besides, a low-power (milliwatt pump power) all-optical wavelength converter with a wide wavelength tuning range is experimentally demonstrated via the coherent anti-Stokes Raman scattering in this multimode waveguide. The pump power is 200× lower than the previous reports with comparable Stokes/anti-Stokes power conversion efficiency. The wavelength converter can operate in the wavelength conversion range of the whole telecom band with a wavelength conversion range of about 220 nm.

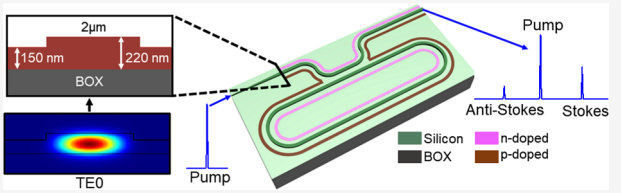

KEYWORDS: *anti-Stokes Raman lasing, milliwatt pump threshold power, low-power all-optical wavelength converter, wide wavelength conversion range, silicon racetrack resonator, nonlinear optics*

Stimulated Raman scattering (SRS) in optical waveguides has attracted much interest[1−5] because of its potential applications in wavelength conversion[6,7] and on-chip Raman spectroscopy.[8−11] It also improves the understanding of the optical physics of high-quality-factor (Q) cavities in terms of Stokes Raman lasers and anti-Stokes Raman lasers.[12−14] Recent interest in integrated Raman lasers has extended to the use of machine-learning methods to design silicon Raman lasers with low threshold powers.[15] Nonlinear wavelength conversion is widely used to produce wavelength differences from a pump laser at either longer or shorter wavelengths and typically relies on nonlinear parametric conversion.[16−18] SRS-based wavelength conversion offers additional advantages of high efficiency that can enable cascaded Raman lasing for wavelength conversion spanning a large wavelength range.[6,19,20] A SRS wavelength converter can convert the pump wavelength to both the Stokes wavelength and the anti-Stokes wavelength via the SRS and coherent anti-Stokes Raman scattering (CARS) covering a wide wavelength conversion range.[19] Silicon as a complementary metal-oxide-semiconductor compatible platform has mature MPW-foundry processes and a high third-order nonlinear coefficient.[21] SRS in silicon platform has been studied extensively, including its use for optical amplification[22,23] and Raman lasers.[24−26]

Compared to Stokes Raman silicon lasers, anti-Stokes Raman silicon lasers have not been well explored. In 2003, in a 1.8 cm long silicon waveguide, anti-Stokes Raman conversion was first demonstrated via the CARS with two pump photons and one Stokes photon.[27] Afterward, with a pulsed pump input, simultaneous Stokes and anti-Stokes emissions were observed in a 2 cm long silicon waveguide.[28] Broadband CARS was observed by the self-phase-modulation-induced spectral broadening of the optical pulsed pump.[29] Rather than using silicon platform, recent progress of anti-Stokes Raman lasers realized the submilliwatt/milliwatt threshold pump powers in metal-doped silica/pure silica microcavities with ultrahigh Qs (>10^7).[30] In a silica microtoroid resonator with an organic monolayer, the stimulated anti-Stokes Raman scattering (SARS) efficiency was increased by 3 orders of magnitude than previous hybrid resonators.[19] Compared with the silica platform, silicon has 2 orders of magnitude larger nonlinear coefficients. However, it suffers from large nonlinear absorptions under high power. Therefore, until now, no experimental demonstrations on continuous-wave (CW) anti-Stokes Raman lasers have been reported in silicon cavities.

In silicon, the anti-Stokes emission from the CARS is highly affected by the Stokes output generation, optical linear absorption, and nonlinear absorptions. Further attaining a CW anti-Stokes Raman laser faces the same challenges. To address these challenges, we are motivated to engineer a highly efficient CW Stokes Raman silicon laser and thus achieve a

Received: August 31, 2021

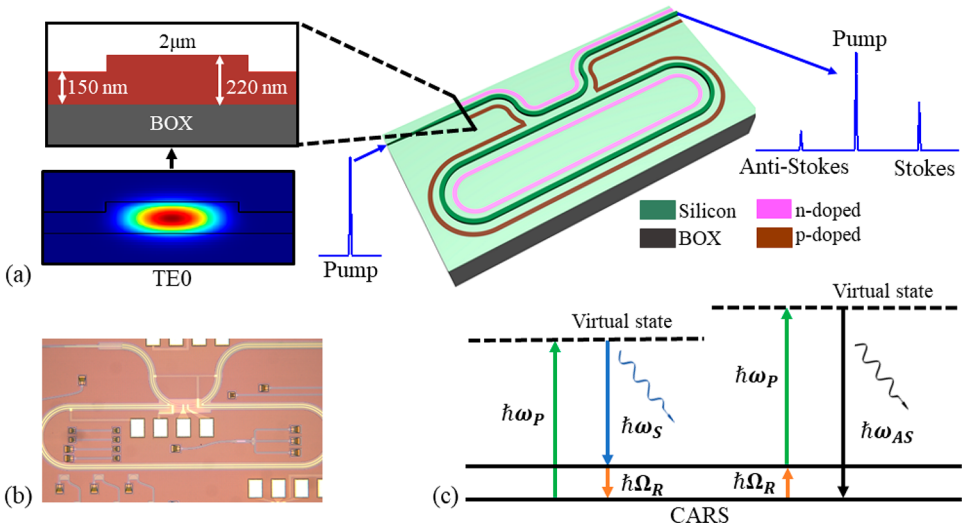

Figure 1. Configuration of the silicon racetrack resonator and energy level diagram of the process of SRS/SARS. (a) Schematic of the silicon racetrack resonator with a lateral p-i-n diode embedded in the waveguide and modal characteristics. The magnified view of the cross-section of the bus waveguide shows the following dimensions: width, 2 μm; height, 220 nm; etch depth, 70 nm. The correspondingly simulated fundamental transverse electric mode (TE0) in the bus waveguide. In the measurement, the pump light is incident to the bus waveguide. The Stokes and anti-Stokes waves generate at the end of the bus waveguide. (b) Microscope image of the resonator with left two metals to apply voltage. (c) Energy level diagrams of the CARS process with the vibrational states of the gain medium. $\omega_P/\omega_S/\omega_{AS}/\Omega_R$: frequency of pump/Stokes/Anti-Stokes/vibrational optical phonon.

CW anti-Stokes Raman silicon laser. Recent interest in using multimode silicon resonators has exhibited large fabrication tolerance and high *Q*s.[31,32] The multimode structure can reduce the interaction between the optical mode and structure sidewalls, leading to low scattering loss from the sidewalls and obtaining high *Q*s.[33] Here, using a racetrack resonator, we engineer all the pump, Stokes, and anti-Stokes wavelengths with high *Q*s (>10^6) to maximally obtain output powers of Stokes and anti-Stokes waves. Moreover, we use the reverse-biased p-i-n diode structure to sweep out the free carriers produced by two-photon absorption (TPA) and then to reduce the nonlinear loss from free-carrier absorption (FCA).[25] For the first time, we present a millimeter-scale CW anti-Stokes Raman silicon laser at a milliwatt level lasing threshold power. The anti-Stokes output power is in good linear proportion to both the Stokes output power and the pump power launched in the fiber. However, even applied with a reverse bias to deplete the free carriers, the Stokes output power starts to saturate with the increase of the pump power. Therefore, the maximum output power of the anti-Stokes wave is hindered as well. Besides, an all-optical wavelength converter with a milliwatt pump power and a wide wavelength tuning range via the CARS process is demonstrated in the silicon waveguide covering the whole telecom band with a maximum conversion bandwidth of 220 nm.

DEVICE STRUCTURE

The resonator was fabricated on a silicon-on-insulator wafer with a silicon thickness of 220 nm by IMEC foundry. The configuration of the racetrack resonator is present in Figure 1a. The cross-section of the bus waveguide includes the waveguide dimensions with width as 2 μm and etch depth as 70 nm. The gap between the bus waveguide and the racetrack is designed as 0.4 μm. The bending radius is designed as 130 μm to have negligible propagation loss from the simulation results with the finite-difference time-domain method.[33] The design of the racetrack resonator is detailed in section 1 of the Supporting Information. The round-trip length of the racetrack is about 2.8 mm. The bus waveguide is 3.8 mm long. Since Raman scattering in silicon results in a 15.6 THz frequency shift from the pump frequency to a lower frequency for the Stokes or 15.6 THz higher frequency for the anti-Stokes waves, two edge couplers are used for light coupling due to their wide bandwidths.[34] The microscope image of the fabricated multimode racetrack resonator is shown in Figure 1b. In the measurement, the pump light is incident to one side of the bus waveguide, and additional Stokes and anti-Stokes waves can be observed at the other side of the bus waveguide.

As shown in Figure 1c, the additional two waves can be explained from the energy level diagram of the processes of SRS and SARS. SRS is a third-order nonlinear process including absorption of a pump photon at the frequency of ω_P and emission of a photon at the Stokes-shifted frequency of $\omega_S = \omega_P - \Omega_R$, together with a phonon excitation at a frequency of Ω_R.[35] Electrons from the virtual state are excited to the vibrational state and then to the ground state. The SRS redistributes the population of the vibrational state. Similar to the SRS process, SARS emission is also a third-order nonlinear process needing a sufficient population of pump and Stokes photons to generate anti-Stokes photons.[30] Thus, compared to the SRS emission, the SARS emission is typically several orders of magnitude lower.[30,36] In the view of the energy level, electrons from the vibrational state are excited to a virtual state and finally go back to the ground state. Generally, anti-Stokes emission is highly correlated with Stokes emission.

Theoretically, the optical intensity of the anti-Stokes wave (I_{AS}) can be obtained with the pump intensity (I_P) and power of the Stokes intensity (I_S) as[30]

$$I_{AS} = \left(\frac{4\omega_P n_2 t}{\varepsilon c}\right)^2 \left(\frac{\sin(\Delta\omega t/2)}{\Delta\omega t/2}\right)^2 \frac{I_P^2 I_S}{A_{eff}^2} \quad (1)$$

where $\Delta\omega = 2\omega_P - \omega_S - \omega_{AS}$ is the frequency detuning, $\omega_P/\omega_S/\omega_{AS}$ is the frequency of pump/Stokes/anti-Stokes wave, n_2

https://doi.org/10.1021/acsphotonics.1c01326
ACS Photonics XXXX, XXX, XXX−XXX

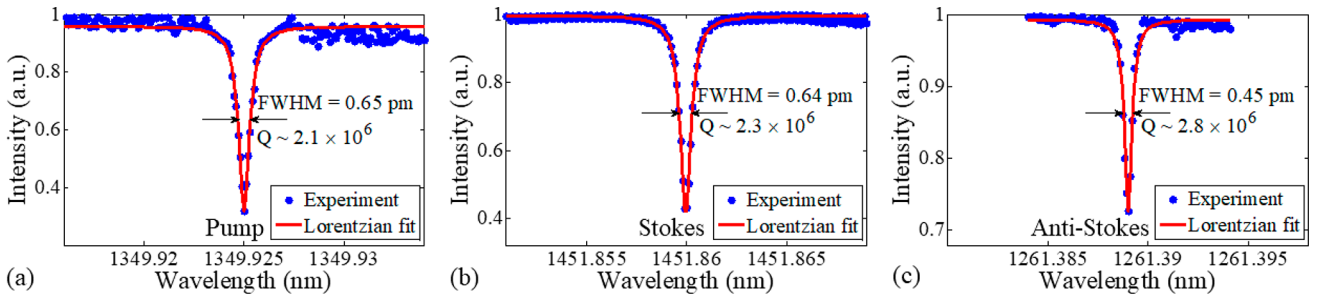

Figure 2. Measured transmission spectra of the pump, Stokes, and anti-Stokes wavelengths. (a–c) Normalized transmission spectra around resonances of 1350 nm used for pump, 1452 nm for Stokes, and 1261 nm for anti-Stokes. *Q*: loaded quality factor; fwhm: full width at half-maximum.

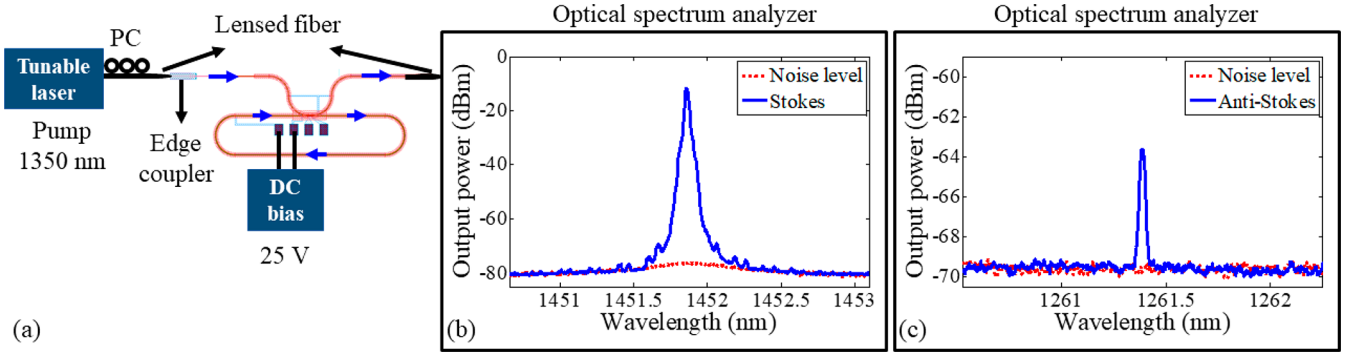

Figure 3. Measured Raman lasing spectra with the experimental setup. (a) Experimental setup for the lasing measurement. Pump light from a tunable laser is coupled into/out of the resonator with two edge couples via lensed fibers. PC: polarization controller; DC: direct current. (b, c) Measured Raman lasing and Raman anti-Stokes lasing spectra with the coupled pump power of 7.1 mW and reverse-biased voltage of 25 V. The spectra of the noise level were recorded by slightly detuning the pump wavelength into off-resonance, showing a broadband peak from the spontaneous Raman scattering.

is the Kerr nonlinear coefficient, t is the interaction time between the pump and the Raman modes, ϵ is the permittivity, c is the speed of light in Raman modes, and A_{eff} is the effective mode area.[19,30] When reaching the Raman lasing threshold, a clamped pump occurs, indicating that the pump intensity inside the resonator I_{P} would keep constant even though the amount of power in the launched fiber increases.[37] Equation 1 shows a clear relation that the anti-Stokes power is in linear proportion to the Stokes power. Besides, since the Stokes power is linearly proportional to the pump power launched in the fiber, the anti-Stokes power is linearly dependent on the pump power launched in the fiber as well.

After the fabrication of the resonator, we first measured the average propagation loss of the resonator as 0.3 ± 0.06 dB/cm. Then we characterized the transmission of the resonator. A CW light with a power of 0.1 mW from a tunable laser was coupled into the bus waveguide. We chose a pump around a resonant wavelength of 1350 nm. According to the frequency detuning of 15.6 THz, we found suitable resonant wavelengths around 1452 and 1261 nm for the buildup of Stokes and anti-Stokes waves. With a wavelength scanning step of 0.1 pm, we measured the transmission spectra around the three wavelengths, as shown in Figure 2. The total insertion losses from fiber to fiber at the pump, Stokes, and anti-Stokes wavelengths were measured as 8.2, 7, and 12.6 dB. The corresponding full widths at half-maximum (fwhm) were measured as 0.65, 0.64, and 0.45 pm with Lorentzian fitting curves. The loaded *Q*s then were calculated as 2.1 × 10^6, 2.3 × 10^6, and 2.8 × 10^6. The propagation losses were calculated from the transmission curves as 0.3, 0.26, and 0.28 dB/cm. The coupling ratios of the directional coupler at these three wavelengths were calculated as 0.54%, 0.35%, and 0.15%.[38] The corresponding enhancement factors were calculated as 35.3, 33.7, and 14.8.

ANTI-STOKES RAMAN LASING MEASUREMENTS

With the experimental setup in Figure 3a, we conducted the SRS and SARS measurements in the resonator. Employing a source meter to apply the resonator with reverse bias, we used a CW tunable laser to generate a pump light and a polarization controller to adjust the light to quasi-transverse-electric polarization. The pump light was coupled into and coupled out of the resonator with two edge couplers via two lensed fibers. We used an optical spectrum analyzer with a resolution of 0.02 nm to record the output spectrum coupled out from the edge coupler. During tuning the laser wavelength into the resonance, we set the laser wavelength with a small detuning from 1350 nm and then increased the laser wavelength with a step of 0.1 pm to achieve the maximum photocurrent, which was monitored as an indicator of the maximum mode interaction with the material (considering the change of the group delay when the light goes across the resonance).[39] When the light is on resonance, the light would experience the maximum buildup of the light intensity and generate the maximum current. When the built-up pump light intensity is larger than the lasing threshold, we can observe a Stokes output from Raman lasing, located on the longer wavelength side of the pump wavelength with about 15.6 THz frequency detuning. From eq 1, anti-Stokes emission depends on both intensities of the pump and Stokes wave. Therefore, we would not observe the anti-Stokes light arising with the Stokes light

https://doi.org/10.1021/acsphotonics.1c01326
ACS Photonics XXXX, XXX, XXX−XXX

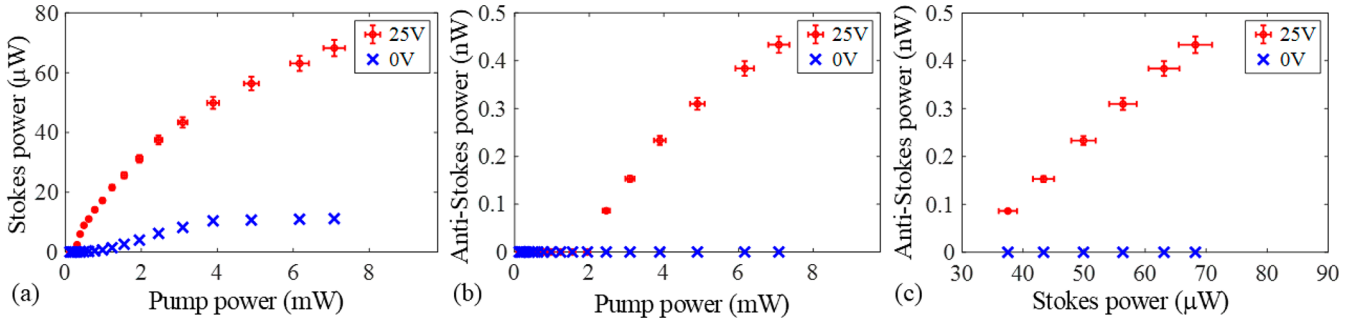

Figure 4. Raman lasing output powers characteristics. Measured (a) Stokes and (b) anti-Stokes Raman lasing output powers as functions of the coupled pump powers. (c) Anti-Stokes output power against Stokes output power. Error bars include the uncertainties for the pump power, the Stokes output power, and the anti-Stokes output power.

simultaneously until the Stokes intensity gradually increases with the pump intensity to a certain value.

In detail, with a reverse-biased voltage of 25 V, we chose a coupled pump power of 7.1 mW. The coupled pump power is the power coupled into the bus waveguide, that is, power in the fiber minus the coupling loss at the input edge coupler. By gradually tuning the laser wavelength into resonance, we observed both Stokes Raman lasing and anti-Stokes Raman lasing at wavelengths of 1452 and 1261 nm, as shown in Figure 3. Since the coupling losses at Stokes and anti-Stokes wavelengths were different, we define the output power as the power in the bus waveguide, before coupling into the output fiber. The corresponding output powers were measured as 68.2 μW and 0.4 nW. It is clear that the intensity of the anti-Stokes emission is several orders of magnitude weaker than that of the Stokes emission as previous reports.[19,30] The noise level spectra were recorded by slightly detuning the pump wavelength into off-resonance, but a little power remained in the resonator. Thus, we can observe a broadband peak around the Raman wavelength, which is the spontaneous Raman scattering with a broader bandwidth than the SRS.[40] With the same pump wavelength at 1350 nm, the second-order Stokes emission was also observed from the OSA at 1570.7 nm (Figure S5, Supporting Information). The output power was measured as −75 dBm, which is lower than that of the anti-Stokes emission.

To verify the relation among the Stokes, anti-Stokes, and pump lights, Raman lasing thresholds for both SRS and SARS emissions were measured as functions of the coupled pump powers with a reverse bias of 25 V and without any bias, as shown in Figure 4. We first plot the SRS power as a function of the coupled pump power shown in Figure 4a. We observed lasing at both 25 bias and 0 V bias with the lasing threshold powers of 0.3 and 0.6 mW. The corresponding SRS efficiencies were measured as 3.8% and 0.3%. For the SRS process, either with 25 V bias or no bias, when the pump power reaches the threshold power, it starts to increase with the pump power, but it gradually saturates. It is due to the large nonlinear losses under a high power circulating inside the resonator where the TPA and FCA would increase linearly and squared with the pump power.[25] Compared to the measurement with 25 V bias, the measurement without any bias exhibits earlier saturation of the Stokes output power. It can be explained by the longer carrier lifetime with no bias, which would lead to the enhanced free-carrier density.[25] It further results in increased nonlinear loss from the FCA and reduces the net gain during SRS emission.

Then, we plot the anti-Stokes output power as a function of the coupled pump power, as shown in Figure 4b. Since the increased power inside the ring would produce heat and further affect the resonant wavelength, readjusting the pump light into the resonance is necessary when changing the pump power. From eq 1, when the anti-Stokes starts to lase, the pump power inside the ring would keep constant and the anti-Stokes power would increase linearly with the Stokes power. Since the Stokes power increases with the coupled pump power in Figure 4a, the anti-Stokes power would show the same increased tendency with the coupled pump power as evidence of the measured anti-Stokes power as a function of the coupled pump power in Figure 4b. With 25 V bias, the anti-Stokes Raman lasing occurs at a threshold power of 2.5 mW, and the SARS efficiency was measured as 1×10^{-5}%. The anti-Stokes Raman lasing is much later than the Stokes Raman lasing since the intensity of the anti-Stokes wave depends on the intensities of both pump light launched in the fiber and Stokes wave from eq 1.

However, we did not observe the anti-Stokes Raman lasing with 0 V. Because the anti-Stokes lasing threshold power was 2.5 mW, and the corresponding Stokes power was 38.4 μW when applied with 25 V bias, which is 3.5× larger than the maximum Stokes power under 0 V bias. Since the anti-Stokes power is linearly proportional to the Stokes power from eq 1, even with the maximum coupled pump of 7.1 mW and ignoring the large nonlinear losses under 0 V bias, it is still impossible to have sufficient Stokes emission to interact with the pump light to generate the anti-Stokes emission. At last, we plot the anti-Stokes output power against the Stokes power, which exhibits a linear relationship shown in Figure 4c, agreeing well with eq 1. Current anti-Stokes output power is highly limited by the small Stokes output power, exhibiting no saturation tendency with current low Stokes power. So, it has the potentiality to get enhanced anti-Stokes output power if we can further boost the Stokes power.

Besides, the use of a directional coupler that is over-coupled at the anti-Stokes wavelength can also increase the anti-Stokes output powers.[20,25] For a Raman laser to have both low threshold and high output power, a directional coupler that is under-coupled at the pump wavelength but over-coupled at the Stokes wavelength is needed. This was demonstrated recently in a Raman laser formed by a chalcogenide resonator and a pulley directional coupler.[41] The pulley directional coupler was under-coupled at the pump wavelength and over-coupled at Stokes wavelength. The pully directional coupler can also suppress the generation of higher-order modes.[42] Another approach using an adjustable directional coupler with a

https://doi.org/10.1021/acsphotonics.1c01326
ACS Photonics XXXX, XXX, XXX−XXX

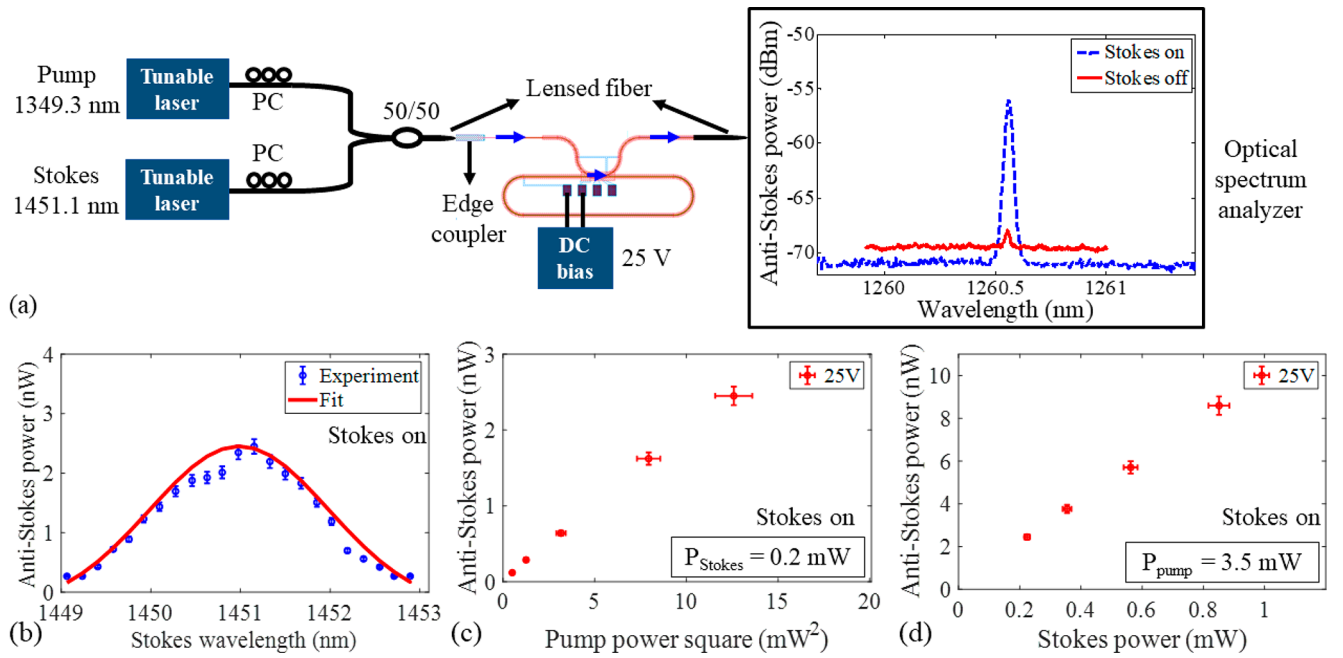

Figure 5. CARS-based all-optical wavelength converter with powers characteristics at reverse-biased voltage of 25 V. (a) Experimental setup for the wavelength converter measurement and the measured Raman anti-Stokes output spectra with and without Stokes input. Two spectra are with different spectral sensitivities for clear comparison. (b) Measured anti-Stokes output powers with varied Stokes wavelengths at coupled pump and Stokes powers of 3.5 and 0.2 mW. (c) Measured anti-Stokes output power as a function of the coupled pump power with a fixed coupled Stokes power of 0.2 mW. (d) Measured anti-Stokes output power as a function of the coupled Stokes power with a fixed coupled pump power of 3.5 mW. Error bars include the uncertainties for the pump power, the Stokes output power, and the anti-Stokes output power.

thermally tuned Mach–Zehnder interferometric structure, can help alleviate the critical dependence of the coupling ratio on the gap size in a conventional directional coupler.[2]

■ ALL-OPTICAL WAVELENGTH CONVERTER

Next, based on the anti-Stokes Raman lasing measurement, we further inject additional input light around the anti-Stokes output. Before the experiment in Figure 5a, we conducted the anti-Stokes lasing measurement again with a pump wavelength of 1349.3 nm to achieve the wavelengths of the Stokes and anti-Stokes. With the coupled pump power of 3.5 mW, the Stokes output is around 1451.1 nm with an output power of 30.2 μW and the anti-Stokes output is near 1260.6 nm with an output power of 0.2 nW as the red solid line of Figure 5a. Then, using the experimental setup in Figure 5a, we injected two inputs at the wavelength of 1349.3 and 1451.1 nm as the pump and Stokes but with 0.05 nm detunings to keep the pump and Stokes inputs inside the bus waveguide rather than the racetrack. Because, in the measurement, when varying one input wavelength, keeping two inputs simultaneously in the resonances is difficult due to the generated heat from the nonlinear effects which would shift the resonant wavelengths. When the lights are off-resonant and mainly propagate in the bus waveguide, the current from the source meter is far below the current when the light is well coupled into the resonance. This could be used to confirm the lights are off-resonant.

With the coupled pump and Stokes powers of 3.5 and 0.2 mW, the measured anti-Stokes output spectrum is shown in Figure 5a using the blue dashed line. The anti-Stokes output power is measured as −56.1 dBm. Then, we fixed the pump wavelength and varied the Stokes wavelength with a 2 nm detuning. With a step of 0.17–0.2 nm, we tuned the Stokes wavelength and recorded the anti-Stokes output power. The anti-Stokes power increases with the Stokes wavelength first and experiences the maximum gain when the Stokes frequency detuning is about 15.6 THz away from the pump wavelength, as shown in Figure 5b. Then it begins to decrease when the Stokes wavelength is beyond 15.6 THz from the pump wavelength. This Stokes-wavelength-dependent anti-Stokes power follows well with the 3 dB line width of 310 GHz for Stokes Raman emission.[27]

At last, we changed the pump power with fixed Stokes power and varied the Stokes power with fixed pump power to measure the anti-Stokes powers. The experimental results are shown in Figure 5c,d, exhibiting the linear relation between the anti-Stokes power and pump power square following the relation between the pump and the idler during the four-wave mixing process rather than being linearly proportional to the pump power during Raman lasing in Figure 4b. It may be evidence that the wavelength conversion stems from the CARS process rather than anti-Stokes Raman lasing.[27,30] With the fixed pump power of 3.5 mW, the anti-Stokes power linearly increases with the Stokes power. The Stokes/anti-Stokes power conversion efficiency was measured as 0.98×10^{-5}, which is comparable with the previous reports but the pump power is 200× smaller.[27] This can be explained by our smaller waveguide core with a lower effective carrier lifetime.[43]

Current Stokes/anti-Stokes power conversion efficiency is mainly limited by the pump power. Since no saturation tendency occurs with the current pump power, further increasing the pump power can highly enhance Stokes/anti-Stokes power conversion efficiency. A similar wavelength converter succeeded in wavelength conversion from the pump wavelength of 1451.2 nm and Stokes signal wavelength of 1570 nm to the anti-Stokes output around 1349.2 nm shown in Figure 6. This CARS-based wavelength converter exhibits low

https://doi.org/10.1021/acsphotonics.1c01326
ACS Photonics XXXX, XXX, XXX–XXX

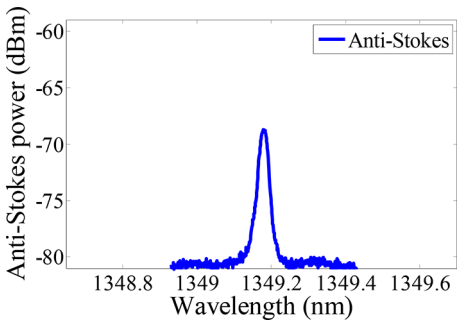

Figure 6. CARS-based all-optical wavelength converter with pump and Stokes wavelengths of 1451.2 and 1570 nm at a reverse-biased voltage of 25 V.

power consumption and a wide wavelength tuning range to cover the whole telecom band with a maximum conversion bandwidth of 220 nm.

CONCLUSION

In conclusion, designing a millimeter-long multimode silicon resonator with high *Q*s at the pump, Stokes, and anti-Stokes wavelengths, we experimentally demonstrate a CW anti-Stokes Raman laser with milliwatt level threshold power for the first time. The experimental results exhibit the anti-Stokes output power has linear dependencies on both Stokes power and pump power launched in the fiber. The measurement applied with 25 V bias achieved the anti-Stokes output, while no anti-Stokes output with 0 V bias, which can be evidence that the silicon resonator suffers from large nonlinear losses under high power circulating inside the cavity. Apart from the single pumped anti-Stokes lasing measurement, we add light around the Stokes wavelength and demonstrate an all-optical wavelength converter with a milliwatt pump power low-power and a wide wavelength tuning range via the CARS process in silicon waveguides. The pump power is 200× smaller than the previous reports with the comparable Stokes/anti-Stokes power conversion efficiency. The wavelength converter has a wide wavelength tuning range to cover the whole telecom band and the maximum wavelength conversion bandwidth of 220 nm. For the anti-Stokes Raman lasing, the Stokes output power starts to saturate with the increase of the pump power, which further limits the maximum anti-Stokes power. Further enhancement of the Stokes power is still needed to increase the anti-Stokes power correspondingly. Reduction of the effective carrier lifetime is an effective approach to decreasing the FCA,[43] which can be a consideration for the further increase of the anti-Stokes output.

ASSOCIATED CONTENT

Supporting Information

The Supporting Information is available free of charge at https://pubs.acs.org/doi/10.1021/acsphotonics.1c01326.

More information about the design of the racetrack resonator, the observed spectrum of the cascaded second-order Stokes emission, and the transmission characteristics with different reverse-biased voltages (PDF)

AUTHOR INFORMATION

Corresponding Authors

Yaojing Zhang − *Department of Electronic Engineering, The Chinese University of Hong Kong, Shatin, New Territories 999077, Hong Kong;* orcid.org/0000-0002-2663-0188; Email: yaojingzhang@cuhk.edu.hk

Hon Ki Tsang − *Department of Electronic Engineering, The Chinese University of Hong Kong, Shatin, New Territories 999077, Hong Kong;* orcid.org/0000-0003-2777-1537; Email: hktsang@ee.cuhk.edu.hk

Authors

Keyi Zhong − *Department of Electronic Engineering, The Chinese University of Hong Kong, Shatin, New Territories 999077, Hong Kong*

Wen Zhou − *Department of Electronic Engineering, The Chinese University of Hong Kong, Shatin, New Territories 999077, Hong Kong*

Complete contact information is available at: https://pubs.acs.org/10.1021/acsphotonics.1c01326

Notes

The authors declare no competing financial interest.

ACKNOWLEDGMENTS

This work was supported by Hong Kong Research Grants Council, General Research Fund (RGC, GRF) (14207117). Y.Z. would like to thank the support from the Postdoctoral Hub-Innovation and Technology Fund (PH-ITF). We would like to thank IMEC for device fabrication, and Synopsys Inc. for making their product Optodesigner available for us to produce the design layout of the photonic circuit.

REFERENCES

(1) Ferrara, M. A.; Sirleto, L. Integrated Raman laser: A review of the last two decades. *Micromachines* **2020**, *11* (3), 330.
(2) Ahmadi, M.; Shi, W.; LaRochelle, S. Widely tunable silicon Raman laser. *Optica* **2021**, *8* (6), 804−810.
(3) Shen, X.; Choi, H.; Chen, D.; Zhao, W.; Armani, A. M. Raman laser from an optical resonator with a grafted single-molecule monolayer. *Nat. Photonics* **2020**, *14* (2), 95−101.
(4) Zhang, Y.; Zhong, K.; Tsang, H. K. Raman lasing in multimode silicon racetrack resonators. *Laser Photonics Rev.* **2021**, *15* (2), 2000336.
(5) Pradhan, A. K.; Sen, M. An integrable all-silicon slotted photonic crystal Raman laser. *J. Appl. Phys.* **2019**, *126* (23), 233103.
(6) Raghunathan, V.; Claps, R.; Dimitropoulos, D.; Jalali, B. Parametric Raman wavelength conversion in scaled silicon waveguides. *J. Lightwave Technol.* **2005**, *23* (6), 2094.
(7) Raghunathan, V.; Claps, R.; Dimitropoulos, D.; Jalali, B. Wavelength conversion in silicon using Raman induced four-wave mixing. *Appl. Phys. Lett.* **2004**, *85* (1), 34−36.
(8) Zhao, H.; Clemmen, S.; Raza, A.; Baets, R. Stimulated Raman spectroscopy of analytes evanescently probed by a silicon nitride photonic integrated waveguide. *Opt. Lett.* **2018**, *43* (6), 1403−1406.
(9) Coucheron, D. A.; Wadduwage, D. N.; Murugan, G. S.; So, P. T.; Ahluwalia, B. S. Chip-based resonance Raman spectroscopy using tantalum pentoxide waveguides. *IEEE Photonics Technol. Lett.* **2019**, *31* (14), 1127−1130.
(10) Tyndall, N. F.; Stievater, T. H.; Kozak, D. A.; Koo, K.; McGill, R. A.; Pruessner, M. W.; Rabinovich, W. S.; Holmstrom, S. A. Waveguide-enhanced Raman spectroscopy of trace chemical warfare agent simulants. *Opt. Lett.* **2018**, *43* (19), 4803−4806.
(11) Raza, A.; Clemmen, S.; Wuytens, P.; de Goede, M.; Tong, A. S. K.; Le Thomas, N.; Liu, C.; Suntivich, J.; Skirtach, A. G.; Garcia-

Blanco, S. M.; Blumenthal, D. J.; Wilkinson, J. S.; Baets, R. High index contrast photonic platforms for on-chip Raman spectroscopy. *Opt. Express* **2019**, *27* (16), 23067−23079.
(12) Yasuda, S.; Takahashi, Y.; Asano, T.; Saito, Y.; Kikunaga, K.; Yamashita, D.; Noda, S.; Takahashi, Y. Detection of negatively ionized air by using a Raman silicon nanocavity laser. *Opt. Express* **2021**, *29* (11), 16228−16240.
(13) Soltani, S.; Diep, V. M.; Zeto, R.; Armani, A. M. Stimulated anti-Stokes Raman emission generated by gold nanorod coated optical resonators. *ACS Photonics* **2018**, *5* (9), 3550−3556.
(14) Kurihara, J.; Yamashita, D.; Tanaka, N.; Asano, T.; Noda, S.; Takahashi, Y. Detrimental fluctuation of frequency spacing between the two high-quality resonant modes in a Raman silicon nanocavity laser. *IEEE J. Sel. Top. Quantum Electron.* **2020**, *26* (2), 1−12.
(15) Kawakatsu, T.; Asano, T.; Noda, S.; Takahashi, Y. Sub-100-nW-threshold Raman silicon laser designed by a machine-learning method that optimizes the product of the cavity Q-factors. *Opt. Express* **2021**, *29* (11), 17053−17068.
(16) Foster, M. A.; Turner, A. C.; Salem, R.; Lipson, M.; Gaeta, A. L. Broad-band continuous-wave parametric wavelength conversion in silicon nanowaveguides. *Opt. Express* **2007**, *15* (20), 12949−12958.
(17) Pasquazi, A.; Ahmad, R.; Rochette, M.; Lamont, M.; Little, B. E.; Chu, S. T.; Morandotti, R.; Moss, D. J. All-optical wavelength conversion in an integrated ring resonator. *Opt. Express* **2010**, *18* (4), 3858−3863.
(18) Xu, X.; Wu, J.; Tan, M.; Nguyen, T. G.; Chu, S. T.; Little, B. E.; Morandotti, R.; Mitchell, A.; Moss, D. J. Broadband microwave frequency conversion based on an integrated optical micro-comb source. *J. Lightwave Technol.* **2020**, *38* (2), 332−338.
(19) Kovach, A.; Gallegos, A.; He, J.; Choi, H.; Armani, A. M. Cascaded Stokes and anti-Stokes laser based on an optical resonator with a self-assembled organic monolayer. *Opt. Lett.* **2020**, *45* (15), 4244−4247.
(20) Rong, H.; Xu, S.; Cohen, O.; Raday, O.; Lee, M.; Sih, V.; Paniccia, M. A cascaded silicon Raman laser. *Nat. Photonics* **2008**, *2* (3), 170.
(21) Zhang, Y.; Cheng, Z.; Liu, L.; Zhu, B.; Wang, J.; Zhou, W.; Wu, X.; Tsang, H. K. Enhancement of self-phase modulation induced spectral broadening in silicon suspended membrane waveguides. *J. Opt.* **2016**, *18* (5), 055503.
(22) Claps, R.; Dimitropoulos, D.; Raghunathan, V.; Han, Y.; Jalali, B. Observation of stimulated Raman amplification in silicon waveguides. *Opt. Express* **2003**, *11* (15), 1731−1739.
(23) Liang, T.; Tsang, H. Efficient Raman amplification in silicon-on-insulator waveguides. *Appl. Phys. Lett.* **2004**, *85* (16), 3343−3345.
(24) Boyraz, O.; Jalali, B. Demonstration of a silicon Raman laser. *Opt. Express* **2004**, *12* (21), 5269−5273.
(25) Rong, H.; Xu, S.; Kuo, Y.-H.; Sih, V.; Cohen, O.; Raday, O.; Paniccia, M. Low-threshold continuous-wave Raman silicon laser. *Nat. Photonics* **2007**, *1* (4), 232.
(26) Takahashi, Y.; Inui, Y.; Chihara, M.; Asano, T.; Terawaki, R.; Noda, S. A micrometre-scale Raman silicon laser with a microwatt threshold. *Nature* **2013**, *498* (7455), 470.
(27) Claps, R.; Raghunathan, V.; Dimitropoulos, D.; Jalali, B. Anti-Stokes Raman conversion in silicon waveguides. *Opt. Express* **2003**, *11* (22), 2862−2872.
(28) Boyraz, O.; Dimitropoulos, D.; Jalali, B. Observation of simultaneous Stokes and anti-Stokes emission in a silicon Raman laser. *IEICE Electron. Expr.* **2004**, *1* (14), 435−441.
(29) Koonath, P.; Solli, D. R.; Jalali, B. Broadband coherent anti-Stokes Raman scattering in silicon. *Opt. Lett.* **2010**, *35* (3), 351−353.
(30) Choi, H.; Chen, D.; Du, F.; Zeto, R.; Armani, A. Low threshold anti-Stokes Raman laser on-chip. *Photonics Res.* **2019**, *7* (8), 926−932.
(31) Zhang, L.; Hong, S.; Wang, Y.; Yan, H.; Xie, Y.; Chen, T.; Zhang, M.; Yu, Z.; Shi, Y.; Liu, L. New-generation silicon photonics beyond the singlemode regime. *arXiv:2104.04239 [physics.optics]* **2021**, na.
(32) Zhang, L.; Jie, L.; Zhang, M.; Wang, Y.; Xie, Y.; Shi, Y.; Dai, D. Ultrahigh-Q silicon racetrack resonators. *Photonics Res.* **2020**, *8* (5), 684−689.
(33) Zhang, Y.; Hu, X.; Chen, D.; Wang, L.; Li, M.; Feng, P.; Xiao, X.; Yu, S. Design and demonstration of ultra-high-Q silicon microring resonator based on a multi-mode ridge waveguide. *Opt. Lett.* **2018**, *43* (7), 1586−1589.
(34) Mu, X.; Wu, S.; Cheng, L.; Fu, H. Edge couplers in silicon photonic integrated circuits: A review. *Appl. Sci.* **2020**, *10* (4), 1538.
(35) Leuthold, J.; Koos, C.; Freude, W. Nonlinear silicon photonics. *Nat. Photonics* **2010**, *4* (8), 535.
(36) Farnesi, D.; Cosi, F.; Trono, C.; Righini, G. C.; Conti, G. N.; Soria, S. Stimulated anti-Stokes Raman scattering resonantly enhanced in silica microspheres. *Opt. Lett.* **2014**, *39* (20), 5993−5996.
(37) Kippenberg, T. J.; Spillane, S. M.; Min, B.; Vahala, K. J. Theoretical and experimental study of stimulated and cascaded Raman scattering in ultrahigh-Q optical microcavities. *IEEE J. Sel. Top. Quantum Electron.* **2004**, *10* (5), 1219−1228.
(38) Xuan, Y.; Liu, Y.; Varghese, L. T.; Metcalf, A. J.; Xue, X.; Wang, P.-H.; Han, K.; Jaramillo-Villegas, J. A.; Al Noman, A.; Wang, C. High-Q silicon nitride microresonators exhibiting low-power frequency comb initiation. *Optica* **2016**, *3* (11), 1171−1180.
(39) Babaghorbani, B.; Kaatuzian, H. Enhancement of slow and fast light devices characteristics, combining ring resonator with fiber bragg gratings. *Optik* **2021**, *228*, 166167.
(40) Claps, R.; Dimitropoulos, D.; Han, Y.; Jalali, B. Observation of Raman emission in silicon waveguides at 1.54 μm. *Opt. Express* **2002**, *10* (22), 1305−1313.
(41) Huang, Y.; Xia, D.; Zeng, P.; Zhao, J.; Yang, Z.; Sun, S.; Luo, L.; Hu, G.; Liu, D.; Li, Y. Engineered Raman lasing in photonic integrated chalcogenide microresonators. *arXiv:2107.11719 [physics.optics]* **2021**, na.
(42) Hosseini, E. S.; Yegnanarayanan, S.; Atabaki, A. H.; Soltani, M.; Adibi, A. Systematic design and fabrication of high-Q single-mode pulley-coupled planar silicon nitride microdisk resonators at visible wavelengths. *Opt. Express* **2010**, *18* (3), 2127−2136.
(43) Claps, R.; Raghunathan, V.; Dimitropoulos, D.; Jalali, B. Influence of nonlinear absorption on Raman amplification in silicon waveguides. *Opt. Express* **2004**, *12* (12), 2774−2780.

https://doi.org/10.1021/acsphotonics.1c01326
ACS Photonics XXXX, XXX, XXX−XXX